applied sciences

MDPI

Article

Comprehensive Optimization and Design of an Electric Vehicle Battery Box Side Profile for Lightweight and Crashworthiness Using a Novel Hybrid Structure

Muhammet Arslan [1,2,*] and Mehmet İhsan Karamangil [2]

[1] Jaguar Land Rover, Banbury Road, Gaydon CV35 0RR, UK
[2] Department of Automotive Engineering, Faculty of Engineering, Bursa Uludag University, 16059 Nilüfer, Bursa, Türkiye; ihsan@uludag.edu.tr
* Correspondence: marslan3@jaguarlandrover.com

Abstract: Lightweighting is a critical focus in the transportation sector, directly enhancing efficiency and significantly reducing costs. In electric vehicle (EV) design, the body surrounding the battery must effectively absorb impact, especially during crashes. This study aims to improve the crash performance of the side profiles in the battery box of an M1 category vehicle. It is based on the crash test in Annex 8D of the ECE R100 regulation. In this study, the safe displacement at which the battery will not deform is set as 20 mm, and the maximum force and energy absorption at this displacement are compared. In total, 33 different electric and hybrid vehicle models were benchmarked in this study. L-shaped geometry and aluminum materials are generally preferred; this study focuses on using glass-fiber-reinforced polymer (GFRP) pultruded profiles to make batteries more durable and lighter. The GF800 material was selected for its superior mechanical strength among glass fiber composites. A virtual tensile test verified its properties. A unique hybrid model combining honeycomb and auxetic geometries was developed, showing a crash performance improvement of ~360% over honeycomb structures and ~88% over auxetic structures. Through multi-objective optimization using artificial neural networks (ANNs), 27 models were analyzed, leading to an optimized design. The final design resulted in the battery box side profile being 23.9% lighter and 38.6% cheaper, and exhibiting a performance 3% higher. This study demonstrates significant advancements in EV safety and cost efficiency, highlighting the practical benefits of innovative material and design approaches.

Keywords: hybrid structure; multi-objective optimization; glass-fiber-reinforced polymer (GFRP); battery box; crashworthiness; pultrusion

check for updates

Academic Editor: Camelia Cerbu

Received: 9 January 2025
Revised: 10 February 2025
Accepted: 13 February 2025
Published: 15 February 2025

Citation: Arslan, M.; Karamangil, M.İ. Comprehensive Optimization and Design of an Electric Vehicle Battery Box Side Profile for Lightweight and Crashworthiness Using a Novel Hybrid Structure. *Appl. Sci.* **2025**, *15*, 2037. https://doi.org/10.3390/app15042037

Copyright: © 2025 by the authors. Licensee MDPI, Basel, Switzerland. This article is an open access article distributed under the terms and conditions of the Creative Commons Attribution (CC BY) license (https://creativecommons.org/licenses/by/4.0/).

1. Introduction

Companies in the automotive sector are focusing on new efforts to reduce fuel consumption and increase the energy efficiency of vehicles. One of the most effective methods for reducing the fuel consumption and emission rates of vehicles is weight reduction [1]. These lightweight efforts should be in line with international safety standards and consider travel comfort.

In the entire transportation sector, various studies have been carried out to reduce weight and more lightweighting is aimed at using different materials, optimization techniques, and methods such as reducing part quantity. For this reason, many studies on lightweighting have been conducted in the literature [2–5]. The issue of lightweighting is becoming more significant, especially due to intensive use in land transportation. Since

energy efficiency is a concept that comes to the forefront today, there is intense focus on electric vehicle studies [6,7]. This intensity is due to factors such as decreasing oil reserves, increasing exhaust gas emissions and, as a result, increasing global warming.

Sustainability is becoming an increasingly crucial aspect of electric mobility. The advancement of electro-mobility is central to European efforts to reduce carbon emissions and enhance urban quality of life. In this study, the current state of electro-mobility in Europe is explored, examining social, economic, and environmental aspects within a circular economy framework, and this study argues that integrating circular economy principles is essential for achieving sustainable decarbonization across the transport, building, and energy sectors [8].

The automotive sector is vital to the economy and society but significantly impacts global emissions and the environment. This study compares the life cycle assessment, well to wheel, of petrol internal combustion engines and battery electric vehicles, analyzing 17 impact categories related to climate change, human health, resource depletion, and ecosystems. The well-to-wheel approach highlights vehicle use stage emissions in urban areas, addressing sustainability concerns and mitigating usage hypotheses and model differences [9].

Electric vehicles (EVs) are pivotal for reducing greenhouse gas emissions and air pollution, enhancing global quality of life. This study compares life cycle assessments (LCAs) and life cycle cost (LCC) analyses of EVs and fossil fuel vehicles. The findings indicate EVs reduce greenhouse gas emissions but increase human toxicity due to metals, chemicals, and energy used in production. Cost analysis shows flexible pricing, with higher initial costs due to battery prices and future uncertainties in gasoline and electricity costs [10].

In electric vehicle studies, batteries are used as the power source and in addition to factors such as distance and weight, many factors related to safety measures are also important. Especially in crash situations, the body surrounding the battery must absorb the impact as best as possible [11]. Therefore, safety aspects are highly important in the design process of electric vehicles. Measures such as robust protection of the battery compartments, the use of materials that absorb impacts, and the minimization of the risk of crash are taken. In this way, electric vehicles are designed according to the required standards in terms of both energy efficiency and safety [12]. They aimed to increase the crashworthiness and reduce the weight of the battery used in electric vehicles by using multiple load topology optimization. Many studies have focused on the crashworthiness and light weight of batteries used in electric vehicles [13–18].

Electric vehicles are often equipped with large traction battery systems, taking into account the endurance range and overall weight [19]. In addition to affecting the power and economic performance of the vehicle, an increase in weight also leads to an increase in kinetic energy during a crash [20–22]. Therefore, the crashworthiness and lightweight design of electric vehicles face tougher challenges. They addressed a multi-objective optimization design for lightweight vehicle body structures and used multi-objective optimization methods to improve structural performance under multiple load cases [23]. Using genetic algorithms and existing design tools, they optimized the durability of the vehicle body structure under various load cases while reducing its weight [24]. An electric vehicle's lightweight and crashworthiness design was carried out via the six-sigma robust design optimization method. The research results show that the best design for mitigation and crashworthiness can be successfully achieved via the six-sigma robust design optimization method. This method provides a balance between weight reduction and crashworthiness while increasing the sensitivity of the design to different variations [25]. The advantages of fiberglass materials are their high strength, low density and flexibility. These properties

make it an ideal option for protecting batteries against side impacts [26,27]. The use of a fiberglass support profile aims to increase the durability of the battery while simultaneously reducing its weight. This positively impacts the performance and energy efficiency of electric vehicles.

In this study, the design, analysis and optimization of a side profile made of fiberglass material were carried out, and the behavior of the support profile in collision situations was evaluated via numerical simulations. GFRP is a composite material that combines glass fibers with thermosetting resin. Different techniques are used for fiberglass production. Pultrusion is a production method used to produce long and continuous fiber-reinforced polymer composite profiles. This method allows the fiber-reinforced polymer material to be uniformly placed in a matrix resin and then shaped by passing it through a mold. It is a method used in the literature [28–32]. Pultrusion is an efficient method for the mass production of long, durable and lightweight composite profiles. This method is ideal for high-strength and lightweight structures used in many sectors, such as the automotive, aerospace, and building industries, and wind energy [33,34]. Furthermore, materials produced by pultrusion are generally corrosion-resistant and have good mechanical performance. Therefore, the pultrusion method enables the production of more robust and efficient products than conventional materials.

In a related study, the crushing response of cage-filled square tubes under quasistatic compressive loading was investigated. Auxetic cage-filled tubes were compared with honeycomb-filled tubes. An alternative tube and an empty tube were designed such that all the structural cages had equal masses. These experimental results were verified computationally. The experimental and numerical results emphasized that the addition of cage structures greatly improved the crashworthiness. Compared with those of the empty tube, the performance of the collision tube was improved by 62.6%, 64.0% and 79.1% of the experimental values and the energy absorption by the addition of the infill cage, respectively [35].

In the development and characterization of innovative materials and structural systems, the adoption of advanced techniques in Inverse Analysis can reduce the necessity for expensive experimental testing. The practice of Small Punch Tests (SPTs) involves assessing material parameters through inverse analysis, which is accelerated and made more economical by employing a model reduction procedure. This methodology is designed to evaluate material parameters within various constitutive models, thereby providing a more adaptable identification framework capable of addressing a wide range of material behaviors [36].

In another study, the authors focused on the design of crashworthy components and a specific structural configuration that provides efficient shrinkage. In recent advances in crash impact energy, crashworthy components have included thin wall structures, honeycomb structures and metallic foam sandwich structures. Honeycomb and metallic foam structures appear to have high specific energy absorption capabilities. However, both structural configurations have shortcomings: namely, honeycomb structures are only capable in one direction, whereas metallic foam structures are highly irregular three-dimensional cell configurations. In the case of octet lattice structures, the twisted lattice structure with a relative density of 20% was able to produce the highest specific energy absorption [37].

In another study, a discrete optimization-algorithm-based hybrid structure was studied on consecutive orthogonal arrays to further improve its crashworthiness. They concluded that thin-walled tubes of different thicknesses have a greater energy absorption capacity than do structures with walls of the same thickness. An efficient method for topology optimization of crash resilience was established [38].

In this study, a unique hybrid structure was created by combining honeycomb and auxetic geometries. Although there are similar studies in terms of hybrid structures, there are no studies that have focused directly on battery boxes. The critical part of this study is how this hybrid structure deforms in the case of a crash. To optimize the battery side profiles in terms of crashworthiness and light weight, an optimization study was carried out using three design variables. For this purpose, the ANN method was used, and the best networks obtained were then optimized with the multi-objective optimization method. The results were verified, and the optimum design was determined by remodeling and analysis with the parameters of the best result. This approach can be applied not only to optimize the battery box side profile, but also to solve similar multi-objective optimization problems.

2. Materials and Methods

2.1. Materials

Since GFRP is not isotropic, it has different mechanical properties in all axes. The material mechanical properties change according to fiber density and orientation. Like in a flow analysis, the fibers are distributed in the structure and the strength differs regionally. In this study, owing to the pultrusion logic, the material will be distributed over the entire component with equal density and behave like an orthotropic material.

In a related study, three different types of pultruded GFRP laminates were fabricated, and the material properties were tested to validate the numerical and theoretical models. The finite element analysis (FEA) results agreed well with the test results and could provide a reference for the design and construction of GFRP structures. As a result of an extensive search and literature review of the mechanical properties of GFRP, GF800 has been interpreted to have the closest mechanical properties to those of aluminum, and the fiber percentage is directly proportional to the strength; therefore, the GF800 material has been selected [39]. GF800 consists of 60.5% fibers and 39.5% matrix. The mechanical properties of GF800 are given in Table 1. The outputs of this study for the GF800 material were used as inputs and mechanical properties of our study as they were validated numerically and experimentally.

Table 1. Mechanical properties of GF800.

Lamina		**Epoxy Resin**		**E-Glass Fibers**	
Definition	**Value**	**Definition**	**Value**	**Definition**	**Value**
E_1	45.95 GPa	Modulus	3.35 GPa	Longitudinal modulus	74.0 GPa
E_2	14.56 GPa	Shear modulus	1.24 GPa	Transverse modulus	74.0 GPa
E_3	14.56 GPa	Poisson's ratio	0.35	Poisson's ratio	0.2
G_{12}	4.5 GPa	Shear strength	75 MPa	Shear modulus	30.80 GPa
G_{13}	4.5 GPa	Tensile strength	80 MPa	Tensile strength	2150 MPa
G_{23}	5.51 GPa	Compressive strength	120 MPa	Compressive strength	1450 MPa
ν_{12}	0.25	Density	1160 kg/m^3	Density	2560 kg/m^3
ν_{13}	0.25				
ν_{23}	0.3				

E-glass fibers are preferred because of their substantial strength-to-weight percentage, ability to withstand corrosion, and flexibility. The specific characteristics of E-glass were investigated as a key reinforcing fiber, and its implications for structural analysis were interpreted [40]. E-Glass, a widely used synthetic fiber, has significant implications for environmental sustainability. Evaluating the production, use and disposal processes is highly important [41].

Epoxy resin, a thermosetting polymer, is the cornerstone of composite material engineering. It is versatile and adaptable for meeting specific requirements [42]. With the ability to be reinforced with various fibers, composites with a wide range of mechanical properties can be created. Epoxy resin is very durable and resistant to environmental factors. Epoxy resins can be used in a variety of industries, including aerospace, automotive and construction. The versatility of epoxy resin makes it an ideal choice for manufacturing components that require high strength–weight ratios, corrosion resistance, and dimensional stability [43]. A suitable application for GFRP with epoxy resin and E-glass fiber reinforcement offers a combination of high strength, stiffness, and lightweight properties, making them ideal for automotive applications.

A virtual tensile test model was set up with a test coupon as shown in Figure 1, and 0°, 90°, and 45° orientations were considered. The initial length of the material used for the strain calculation is 21.113 mm, which is calculated between the defined nodes. The test coupon section width is 7 mm and thickness is 3 mm. A quad-type mesh with a 0.5 mm element size was implemented.

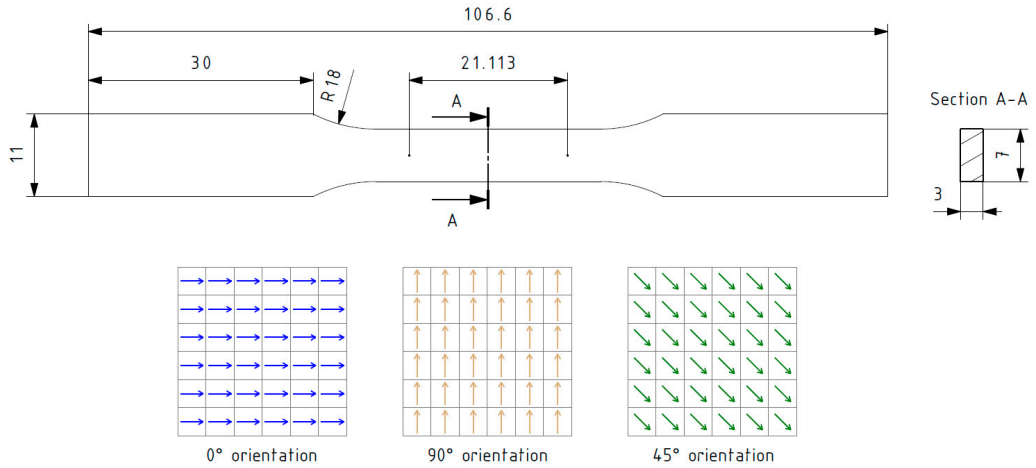

Figure 1. Test coupon and orientations.

In the stress–strain calculation, the linear portion of the curve is the elastic region, and the slope of this region is the elasticity modulus. In these analyses, the slope of the linear portion was taken into account, and the defined material was virtually verified at 0°, 90°, and 45° orientations by obtaining R-square values between 0.99 and 1. The results are given in Table 2.

Table 2. R^2 values of virtual tensile test.

Orientation	Slope of Linear Portion	R^2
0°	y = 45005x + 7.1842	0.9999
90°	y = 14674x + 0.8617	0.9908
45°	y = 12805x + 1.7288	0.9955

R^2 values closer to 1 indicate that the virtual tensile model, in addition to the material card that will be used for FEAs, is accurate.

For material card preparation for FEA, the fiber pultrusion direction is selected as the composite E_1 direction (0° orientation). The structure was represented as five layers for the stress results, and all the layers were in the 0° orientation. Thickness values on the geometric data were used. LAW25 was preferred because it has been successfully used in many studies as a composite model in Radioss Explicit solution [44,45]. LAW25 is the most

commonly used composite material in Radioss. It can be used with shell and solid elements. The two formulations available in LAW25 are the Tsai-Wu and CRASURV formulations. The CHANG failure mode was preferred for this model.

2.2. Benchmarks

In total, 33 different electric and hybrid vehicle models were scanned for electric vehicle (EV) batteries via the A2MAC1 reverse engineering application, and the L structure is generally preferred, as shown in Figure 2.

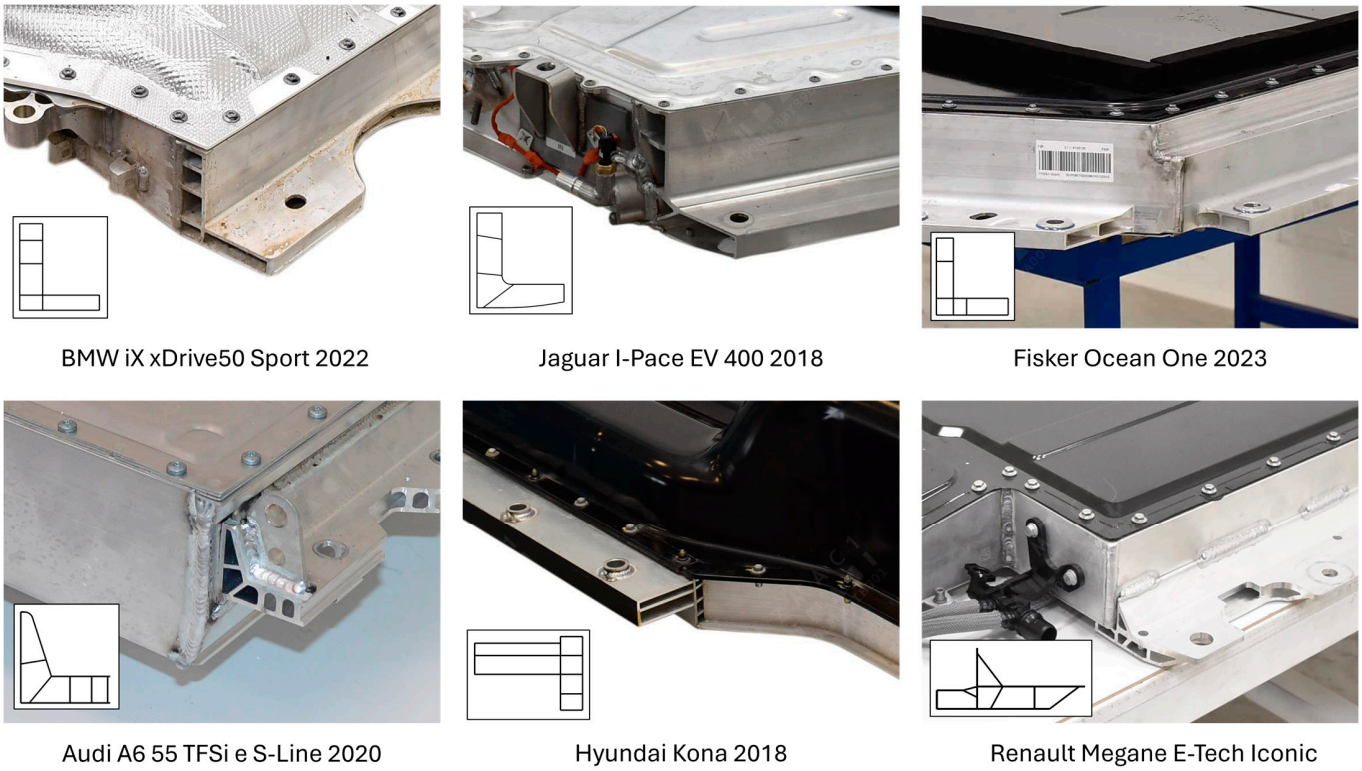

Figure 2. L-shaped structure observed in benchmark studies.

The principal findings from the benchmarked models, specifically regarding material type, side profile dimensions, and thickness range, are presented in Table 3.

Table 3. Key findings' comparison from the benchmarked models.

Vehicle Model	A2Mac1 Ref	Part (s) Weight (kg)	Material Code (s)	Battery Dimensions Width × Height × Depth (mm)	Approx. Side Profile Dimensions Height × Width (mm)	Thickness Range (mm)
BMW iX xDrive50 Sport 2022	2149-387	648.5	AlMg0.7Si AlSiMg AlMg3 PP-GF25 Steel	1730 × 320 × 2410	106 × 132	3.5–4.5
Jaguar I-Pace EV 400 2018	1079-610	603.0	Alloy Plastic Other	1455 × 285 × 2310	135 × 115	3.9–4.8
Fisker Ocean One 2023	2382-679	590.4	Aluminum Plastic	1535 × 165 × 2210	82 × 83	4–5
Audi A6 55 TFSi e S-Line 2020	1896-2303	132.8	EN-AW-6005 AlMgS1 AlSi1.2Mg0.4	1000 × 135 × 690	67 × 65	3–4.5
Hyundai Kona 2018	1114-927	450.4	Other	1440 × 310 × 1970	64 × 95	3–3.7
Renault Megane E-Tech Iconic	2227-497	389.0	Aluminum Steel	1460 × 335 × 1990	50 × 108	4.9–6.2

The existing L structure was redesigned with 90% similarity, as shown in Figure 3, in order to protect the existing know-how of the product and it was determined that aluminum 6082 material is generally used. In this study, the energy absorption and displacement in the current situation were analyzed, and the over-engineering status was interpreted.

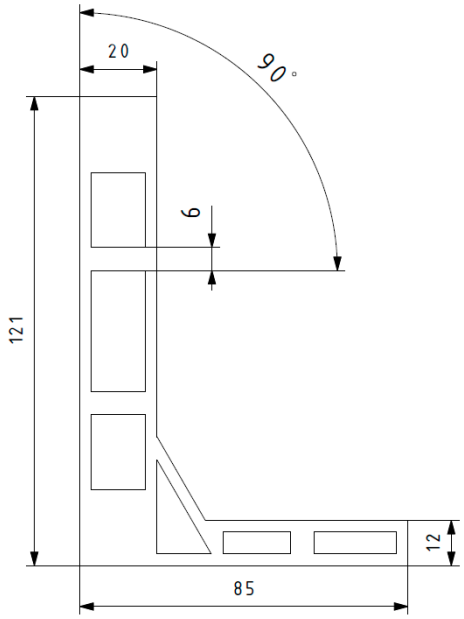

Figure 3. Current model designed on the basis of benchmarks.

2.3. Test Requirements and Heat Dissipation

This study aims to improve the crash performance of the side profiles in the battery box of an M1 category vehicle. The crash test for the battery, according to Annex 8D of the ECE R100 regulation, is summarized. A complete battery pack, including the top cover and bottom base, is subjected to a load of 100 kN with a crushing plate with a radius of 75 mm. Considering the extra strength that other support parts, such as the inner beams and battery cover, add to the system, the maximum safe displacement at which the side profiles can move and the battery will not be deformed is determined to be 20 mm. The pick force and energy absorption at this displacement are compared to prevent over engineering of the structure.

In battery pack research, crashworthiness and heat dissipation are important points and must be considered first when new materials or new structure integrations are used to design side battery box profiles.

In a related study, the crashworthiness and heat dissipation of a design with auxetics in side crash cases were investigated [17]. The NPR-CTP (non-module battery pack with a negative Poisson's ratio) system has better crashworthiness and heat dissipation than other conventional pack systems do, and the comprehensive performance of the optimized NPR-CTP system is effectively strengthened. In another study, the impact of thermal cycles on GFRP pultruded profiles with different geometries was investigated. The bending samples consisted of I-shaped and U-channel profiles that were tested via three-point bending along [46] both the principal weak and strong axes, whereas the box profiles and laminates were utilized in compression and tension tests, respectively. The results demonstrated that the number of thermal cycles has a major impact on the strength of the resin and a minor impact on the strength of the fibers [47].

2.4. Structure Design

In a related study, a hybrid structure combining regular honeycomb and auxetic structure was studied on 3D printed samples. The deformation and failure modes of the different cells and their performance were investigated. Compared with the honeycomb and auxetic structures, the new hybrid structure had better mechanical properties. The compressive strength of the hybrid structure is ~300% greater than that of the honeycomb structure and ~65% greater than that of the auxetic structure. Compared with other structures, the new design is able to absorb more energy [48].

In another study, a new 3D hybrid lattice structure was developed using auxetic and honeycomb, and simulations were conducted on these structures to investigate and compare their energy absorption characteristics. The results show that there are significant improvements. The smallest value of energy absorption under tensile loading was 86% greater than the largest value under compressive loading. Research has indicated that the stiffness and energy absorption of traditional 3D auxetic structures can be improved by combining auxetic and honeycomb structures [46].

In this study, a novel approach is presented that differs from that in the literature. As shown in Figure 4, a hybrid model was created that combines honeycombs and auxetic. This study is unique in that hybrid modeling was developed. The design variables are defined as the maximum edge length (p1), wall thickness (p2) and plane angle (p3).

To understand and verify the development condition of the hybrid model, FEA was performed for all three conditions. A 100 kN force was applied in the compression direction to the fixed panels and displacements were taken into account to compare performance. The panel dimensions were 500 × 500 × 50 mm, and the material was determined as glass fiber. The FEA results are given in Figure 5. The displacement at 100 kN is 13.8 mm for the honeycomb structure, 6.56 mm for the auxetic structure, and 4.82 mm for hybrid structure. The maximum von Mises stress in the honeycomb structure is 131 MPa, that in the auxetic structure is 75.2 MPa, and that in the hybrid structure is 52.4 MPa. In terms of displacement and stress distribution, the hybrid structure is the best choice compared with the honeycomb and auxetic structures.

Crash performance was calculated as the displacement divided by the mass. These units require displacement per weight, which means that the lowest value provides the best performance. On the basis of calculations given in Table 4, the performance value for honeycombs is 0.002233 mm/g, that for auxetics is 0.000911 mm/g, and that for hybrid structures is 0.000485 mm/g. It has been determined that the hybrid structure has a better crash performance. The performance of the new hybrid design is ~360% greater than that of the honeycomb structure and ~88% greater than that of the auxetic structure.

Table 4. Performance comparison of honeycomb, auxetic and hybrid structures.

Lattice Type	Mass (g)	Displacement (mm)	Performance (mm/g)
Honeycomb	6181	13.8	0.002233
Auxetic	7198	6.56	0.000911
Hybrid structure	9936	4.82	0.000485

To investigate the impact of the new hybrid structure on the battery box side profile, lattice structures were generated with design variables that are subject to the following lower and upper limits:

$$60 \text{ mm} \leq \text{p1} \leq 100 \text{ mm}$$

$$6 \text{ mm} \leq \text{p2} \leq 12 \text{ mm}$$

$$15^\circ \leq \text{p3} \leq 135^\circ$$

Second, as shown in Figure 6, battery box side profile sections were generated by trimming the hybrid lattice structures generated with design variables and the outer contours of the current model from each other. The thickness of the outer contour of the current model was maintained. The structure created by providing thickness over the sketch is beneficial in parameter management and enables the middle surfaces to be determined automatically while creating the mesh structure.

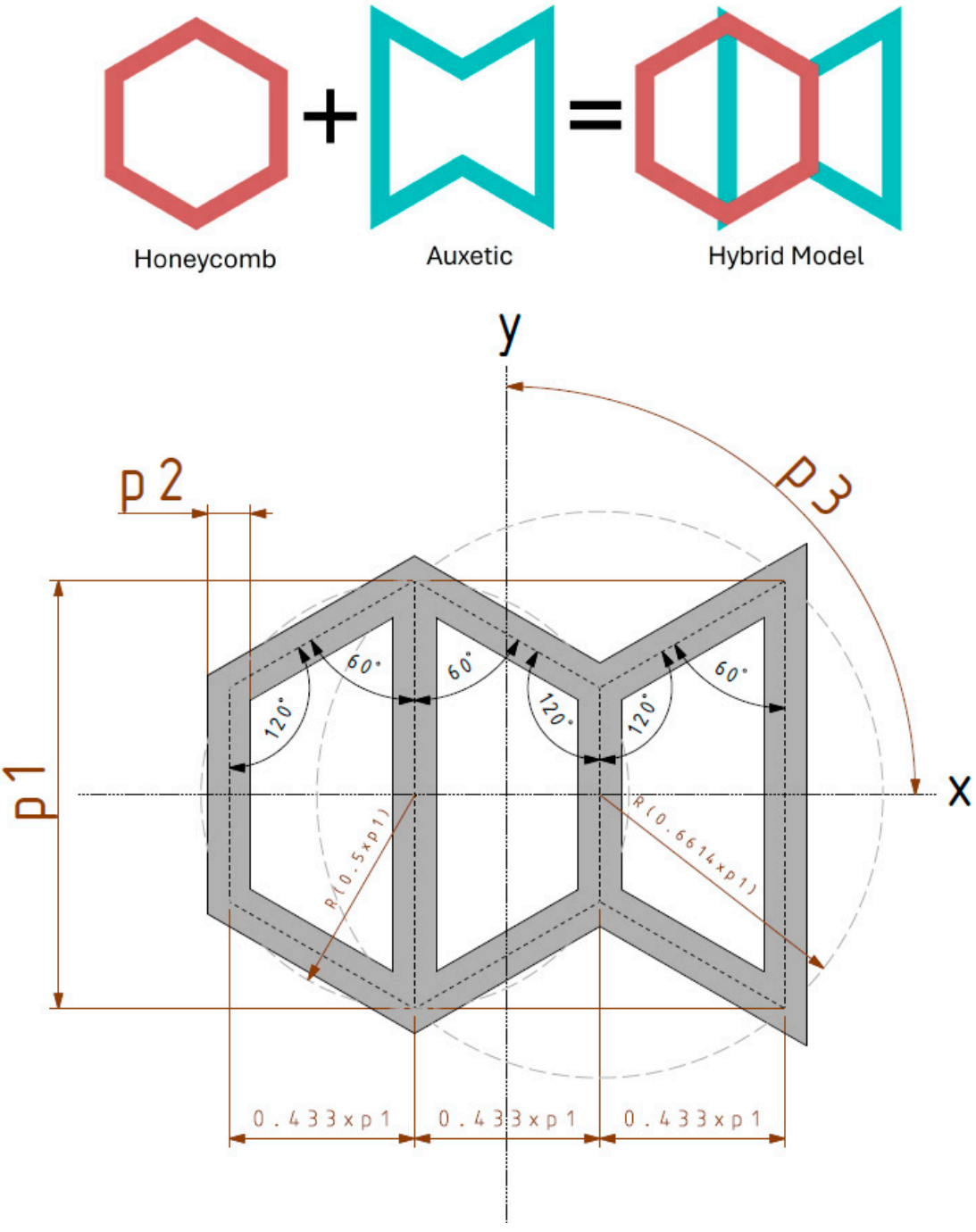

Figure 4. Technical drawing of the hybrid model with design variables.

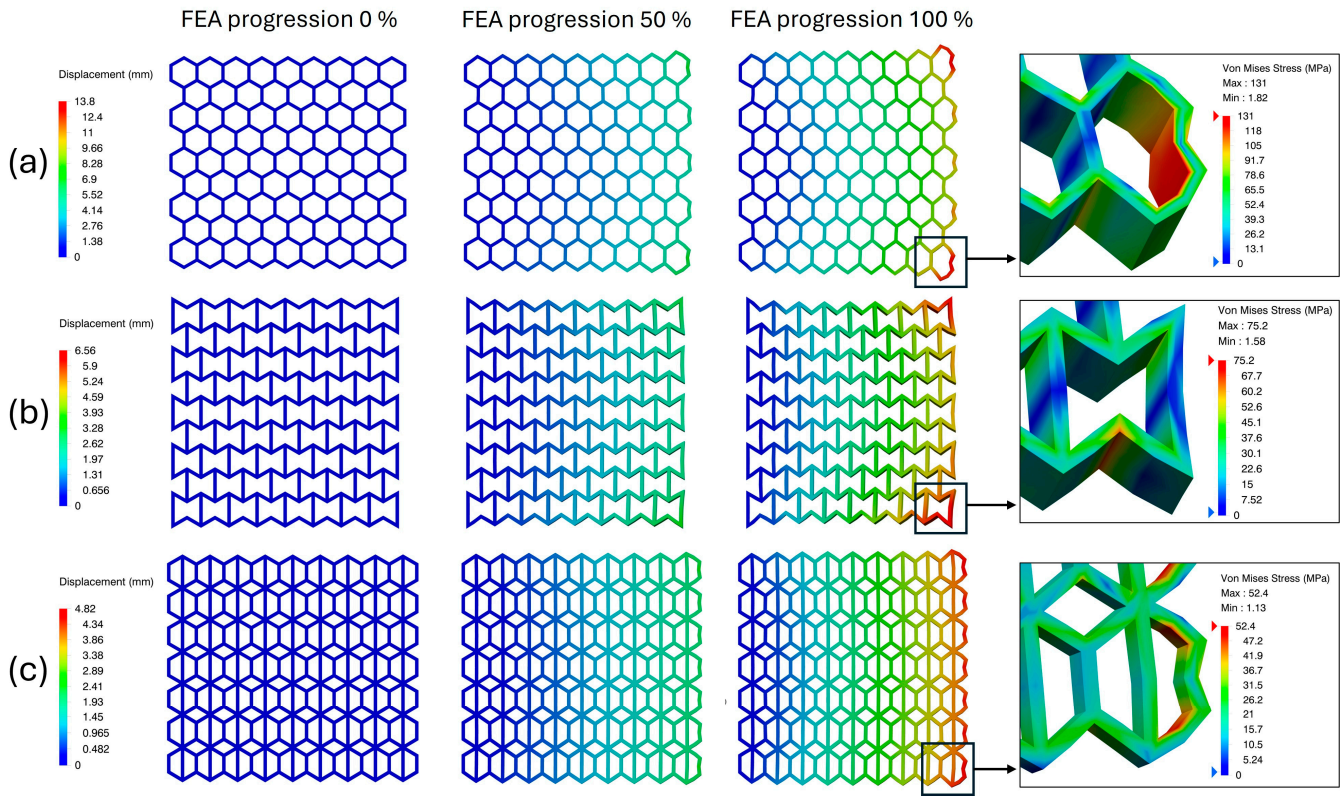

Figure 5. Deformation of 2D lattice structures under compression: (**a**) honeycomb, (**b**) auxetic, and (**c**) hybrid structures.

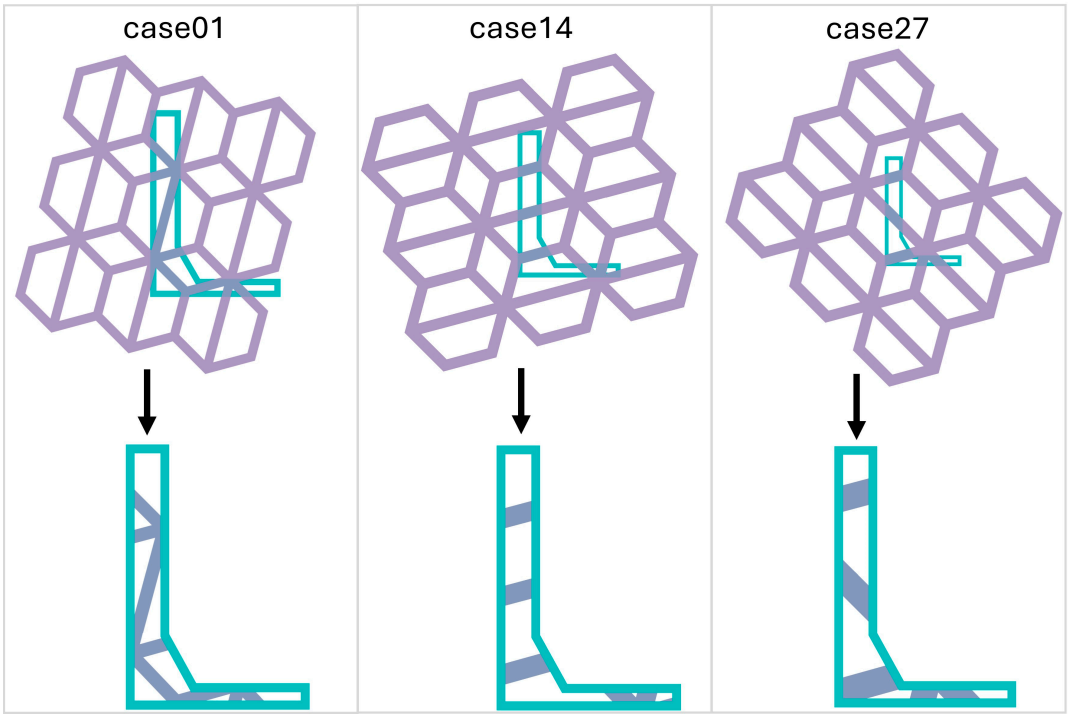

Figure 6. Model creation method for 3 different cases.

A total of 27(3^3) different sections were created by 3dx Catia via a parametric design tool, and all the sections are shown in Figure 7. FEA of these 27 sections was performed to examine the impact of the design variables.

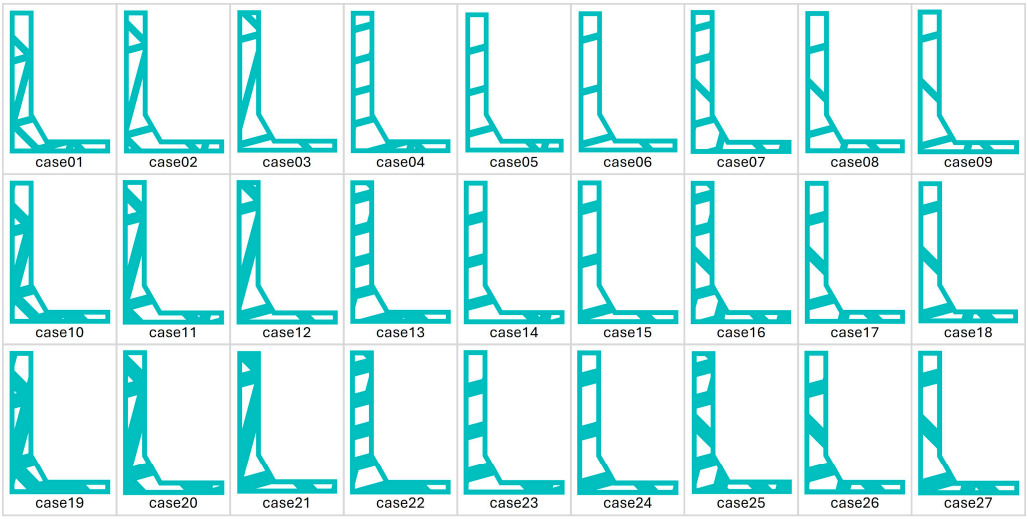

Figure 7. Sections of 27 cases generated with parameters.

2.5. Finite Element Analysis (FEA) Model

The HyperMesh-Radioss interface was used to perform the FEA. The aim was to investigate the structural performance of the battery box side profile. Battery box views and the FEA scenario are shown in Figure 8. The inner beams inside the battery pack that support the side profiles were modeled as 100 mm and fixed with 6 degrees of freedom (DOFs). The material for the inner beams was defined as Al 6082-T6. The connection between the side profile and the inner beams was defined as Type2 (spring). The material for the side profile was defined as GF800. Based on the mesh quality analysis, side profile sections were meshed with 3 mm quad-type elements, ensuring optimal accuracy for strain and stress calculations while maintaining computational efficiency. The connection between the crush plate and the side profile was defined as Type7. The crush plate was modeled rigidly. The load for the FEA model was defined as forced displacement and was applied to the side profile at a constant velocity imposed. The safety margin where the side profiles can move a maximum, that is, the battery will not be deformed, was determined to be 20 mm, and the pick force and energy absorption at this displacement were compared. This FEA model was applied to all 27 cases.

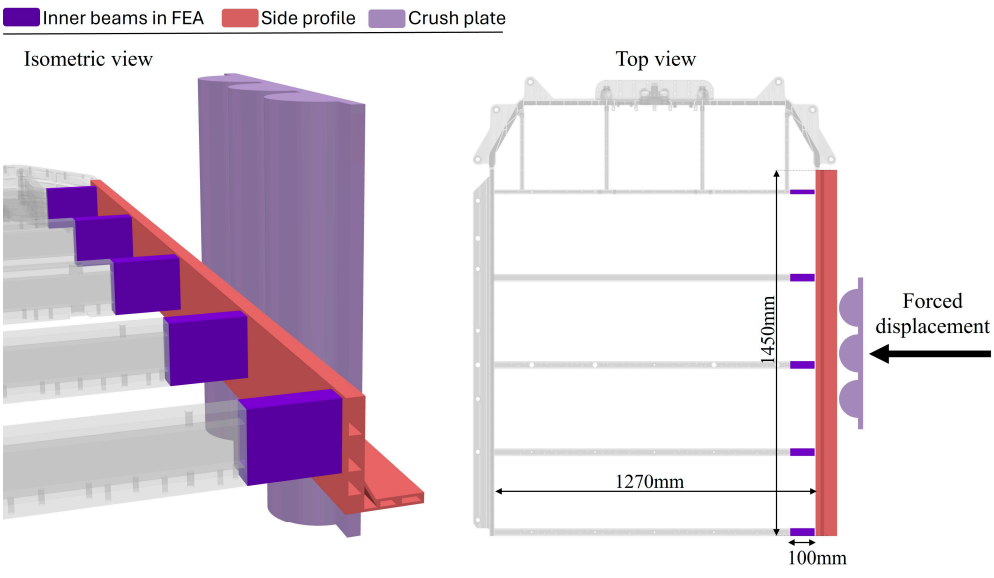

Figure 8. Battery box views and FEA scenario.

2.6. Optimization

Within the scope of the design optimization study, FEA of 27 cases was performed to examine the effects of three design variables. The obtained FEA results were processed and optimized via the MATLAB R2022b program. The flowchart of optimization is shown in Figure 9 and the optimization steps below were carried out.

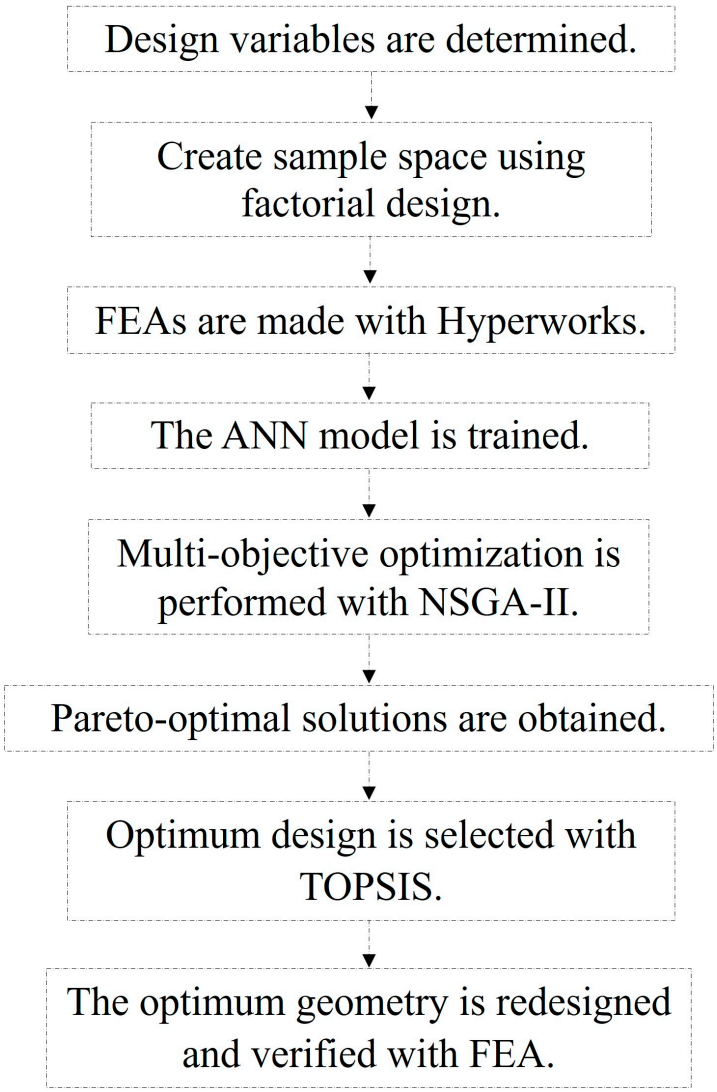

Figure 9. Flowchart of optimization.

First, the design variables (p1, p2 and p3) and the lower and upper values for each parameter were defined. The sample space was created via a factorial design. Twenty-seven different configurations were determined and obtained with the parametric design. Pick force and energy absorption values were obtained for each design.

Next, a modeling approach using artificial neural networks (ANNs) was selected. ANNs were trained to learn the relationships between the design variables and the FEA results. In this way, robust models were created for the influence of design variables and the prediction of FEA results. The input data were used to predict the performance of the battery box side profiles. The ANN was trained with training data and then verified with test data (70% of the data were used for training, 15% for validation and 15% for testing, which were performed randomly).

The trained ANN model was subsequently combined with a multi-objective optimization method. In this study, a multi-objective optimization technique was used to find the

optimal combination of design variables. Multi-objective optimization aims to optimize multiple objective functions simultaneously. The optimal result contains the design variable values that best satisfy the specified objective functions. The objective function of the optimization is to maximize the mass gain and maintain the strength at a sufficient and safe level without over-engineering. Optimization was performed via the nondominated sorting genetic algorithm-II (NSGA-II), a popular multi-objective optimization algorithm known for its fast and specific approach [49,50]. NSGA-II can find a set of Pareto-optimal solutions that represent the best trade-offs between conflicting objectives.

Finally, determining the best outcome on the Pareto front curve resulting from multi-objective optimization requires a preferred decision mechanism or method. This decision mechanism is often referred to as "solution selection" and is determined depending on the requirements, objectives and preferences of the design problem. For this reason, the TOPSIS (Technique for Order of Preference by Similarity to Ideal Solution) method, which is frequently used in solving multifaceted decision making problems, is used in this study [51]. This method evaluates alternative solutions on the basis of different criteria and helps to determine the best solution.

2.6.1. Objective Function

In this study, the optimization objectives considered were peak load minimization (objective 1), mass minimization (objective 2), and maximization of the absorbed energy (objective 3). The objectives were considered equally effective; so, these objectives were combined in this study. This objective function was used to obtain the optimum geometry.

$$\text{Objective function} = 0.33(\text{Objective 1}) + 0.33(\text{Objective 2}) + 0.33(\text{Objective 3}) \quad (1)$$

2.6.2. Modeling with ANN

ANNs are designed to learn the complex relationships between input parameters (P1, P2, P3) and output parameters (mass, peak force (PF), and absorbed energy (AE)).

As shown in Figure 10, the architecture of the ANN model is composed of 3 neurons in the input layer, 15 neurons in the hidden layer, and 3 neurons in the output layer. The Levenberg–Marquardt back-propagation algorithm was used for training the network [52].

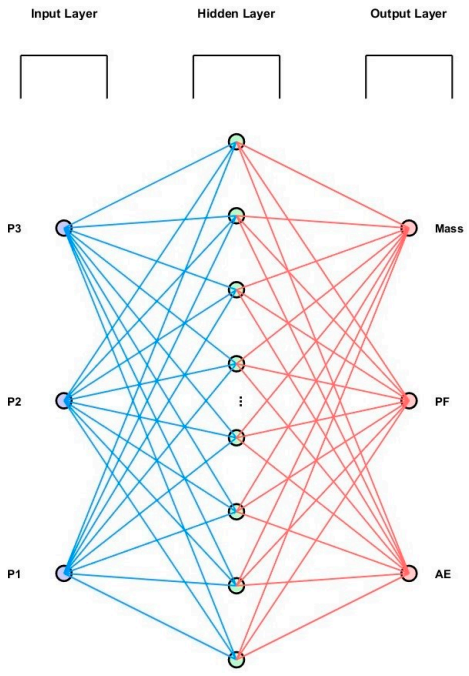

Figure 10. ANN.

The dataset was randomly divided into training (70%), validation (15%), and test (15%) sets. This division was performed to increase the generalization ability of the model and to avoid overfitting.

2.6.3. NSGA-II

After the ANN models were trained, the optimization process was carried out via the multi-objective genetic algorithm (MOGA). The MOGA is an evolutionary algorithm used to optimize multiple objectives simultaneously [53]. In this study, the NSGA-II aimed to determine the optimal design variables using the predictions of ANN models, and the population size was 100 in the implementation of the NSGA-II. The algorithm aims to optimize three objectives simultaneously. The fitness function of the NSGA-II was calculated via the average of the predictions of 50 ANN models. This approach aims to obtain more reliable results by using the collective prediction of many models rather than relying on a single ANN model. A set of Pareto-optimal solutions was obtained at the end of the optimization process. These solutions are in a trade-off relationship with each other and ensure comprehension into the optimal design space and support the selection of the most appropriate combination of input parameters on the basis of desired performance criteria.

2.6.4. TOPSIS

The TOPSIS method was used to select the best-balanced solution among the Pareto-optimal solutions generated by NSGA-II. TOPSIS is a technique used in multicriteria decision-making problems and ranks alternatives according to their similarity to the ideal solution [54]. At the end of this process, the solution that provides the best balance among the Pareto-optimal solutions is identified.

3. Verification

3.1. Final Design and Verification of the Model with Optimal Parameters

The optimized section is presented in Figure 11, and all dimensions are in mm. It was designed with the parameters according to iteration No. 32 in the 3dx Catia program.

The optimized section was reanalyzed for verification, as shown in Figure 12. A detailed comparison is presented in the Results and Discussion section.

3.2. Schematic Representation of the Matrix–Fiber Ratio

The optimized section consisted of a combination of three different materials, namely, E-glass fiber (9600Tex) with a thickness of 1.368 mm, epoxy resin with a density of 1160 kg/m^3, 180 g/m^2 and 0.117 mm thick fabric surrounding the matrix and fiber structure. A schematic representation of the matrix–fiber ratio is given in Figure 13. The fiber ratio in the model is 60.5%, and the matrix ratio is 39.5%.

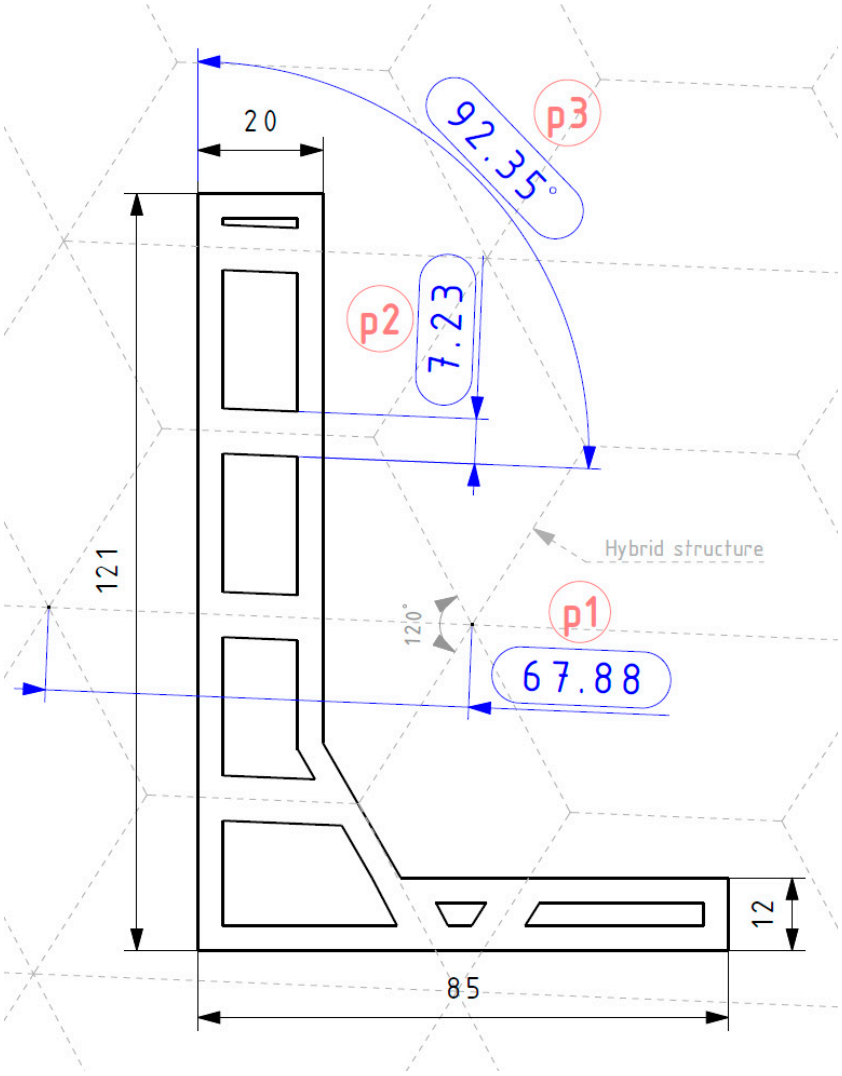

Figure 11. The optimum model is designed as per iteration 32.

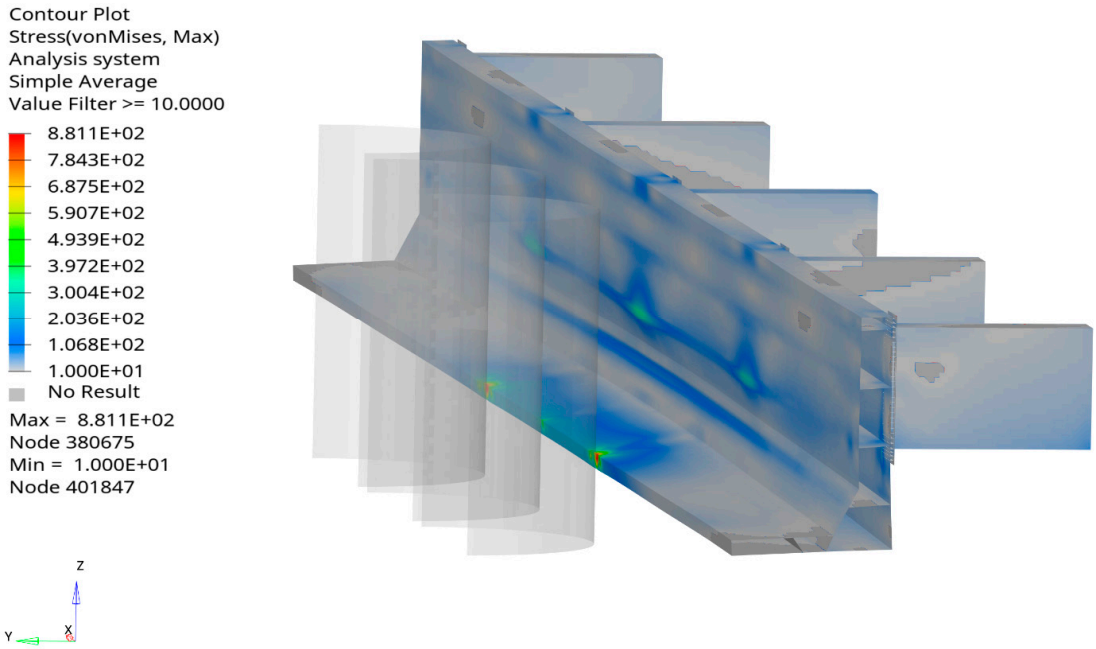

Figure 12. FEA of the optimum model.

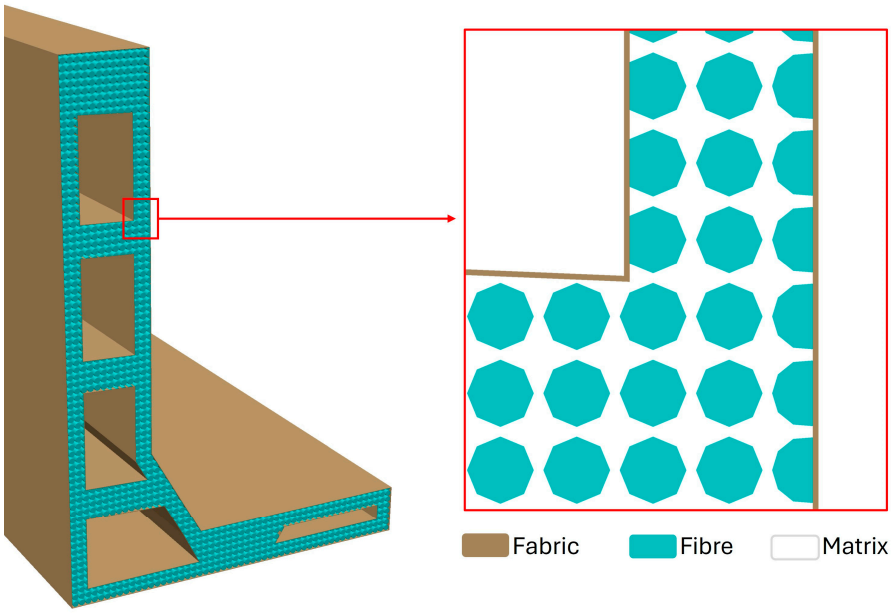

Figure 13. Schematic representation of the matrix–fiber ratio.

4. Results and Discussion

4.1. Current Situation Analysis

As a result of the current model FEA, the pick force was 56,427 N, and the absorbed energy was 840 J. The force–displacement curves of the current model and optimized model are shown in Figure 14. On the basis of literature reviews regarding the mechanical behavior of the Al 6082-T6 profile [55,56], it was assumed that the current model can meet the test requirements of annex 8D of the ECE R100 regulation when a complete battery pack including the top cover and the bottom base is considered. The approach in this study is to avoid over-engineering, which does not provide value, and the overcost structure is simplified. In other words, resources such as material, time and money are generally wasted in terms of value engineering.

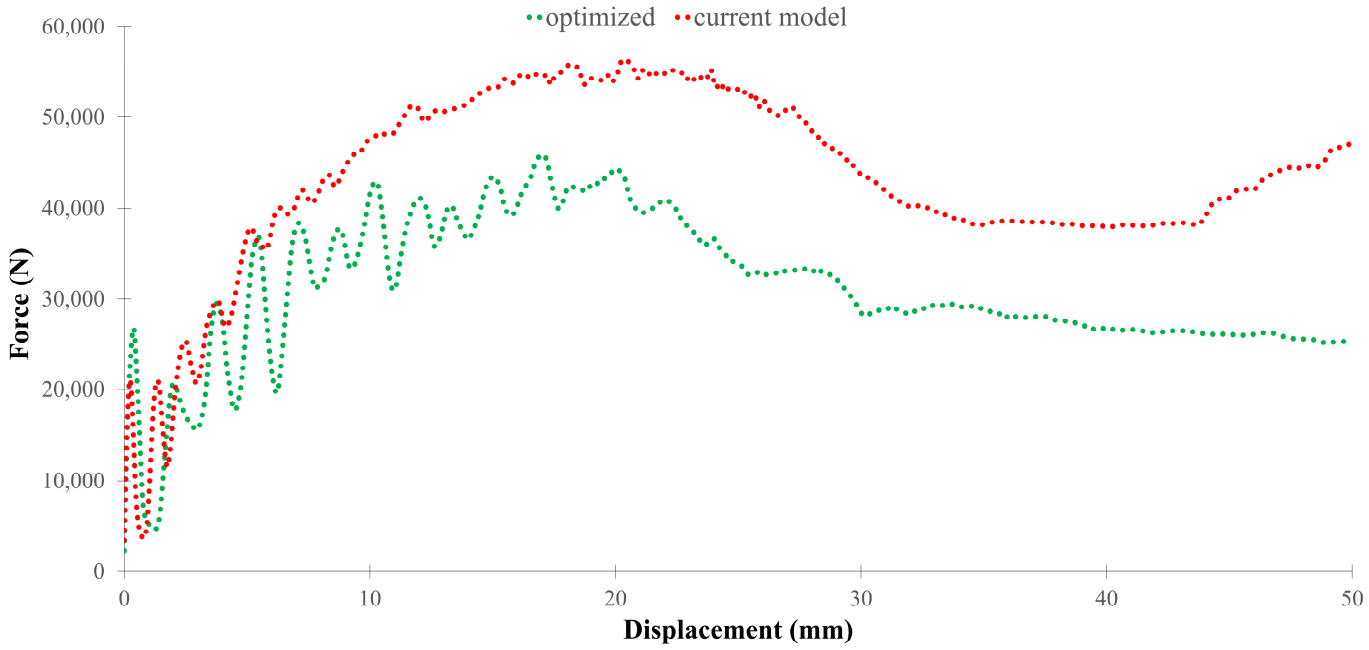

Figure 14. Force–displacement curves of the current model and optimum model.

4.2. Results of FEAs

By analyzing 27 cases and the optimized model, the pick force and energy absorbed up to 20 mm displacement required for optimization were obtained. For the FEA screen and understanding of deformation, case 4 is given in Figure 15 as an example. The FEA results are listed in Table 5, and the force–displacement curves are shown in Figures 16–18. According to the results of the FEA, the case with the highest strength is determined as case 19 and the case with the lowest strength is determined as case 15. The parameters that are prioritized for optimization are determined by the coefficient and the best result is obtained according to the formula. Since the main issue in this study is lightweighting, the mass is minimized, and the absorbed energy is maximized.

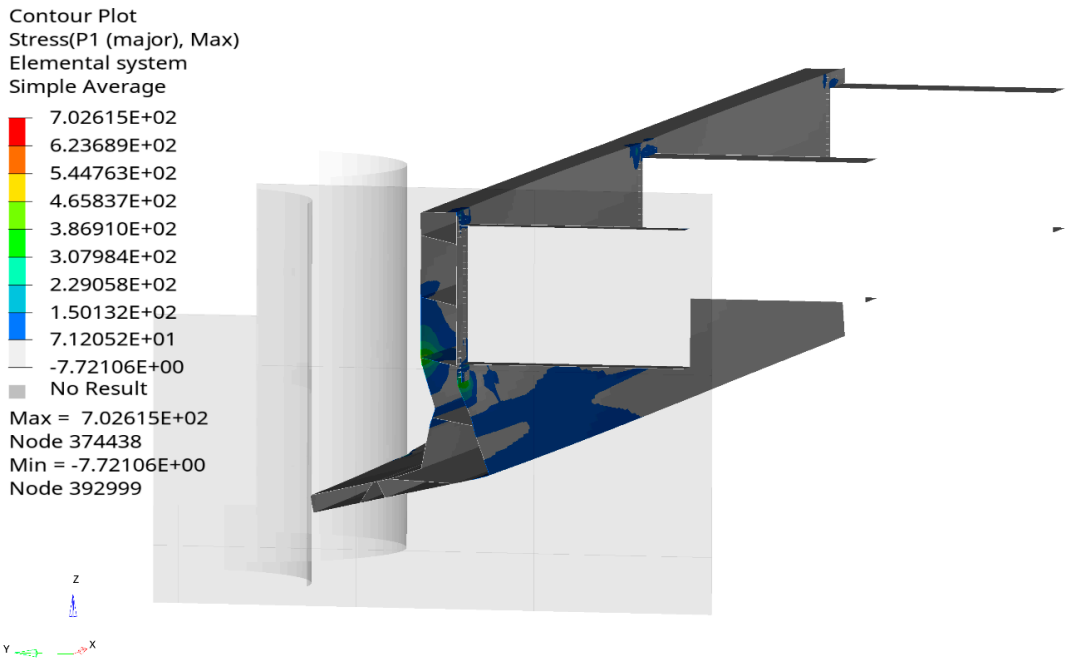

Figure 15. Analysis results for case 4.

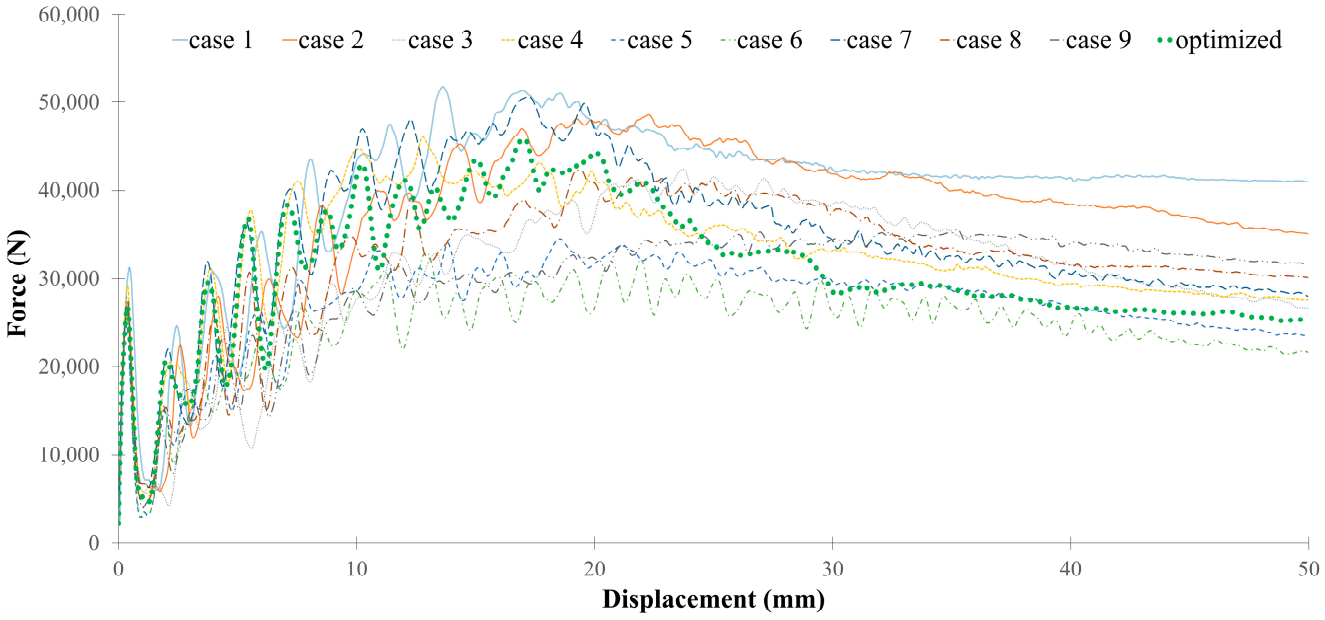

Figure 16. Force–displacement curves of cases 1–9 and the optimized model.

Table 5. FEA results for 27 different cases.

Case No.	Design Variables			Objectives		
	p1 (mm)	p2 (mm)	p3 (degree)	Mass Gain (g)	Pick Force (N)	Absorbed Energy (J)
case 1	60	6	15	871	51,772	730.6
case 2	80	6	15	1164	48,611	643.6
case 3	100	6	15	1392	42,438	509.2
case 4	60	6	75	1829	46,099	688
case 5	80	6	75	2209	34,529	505.9
case 6	100	6	75	2195	32,985	462.5
case 7	60	6	135	1785	50,652	727.4
case 8	80	6	135	2129	42,363	569.1
case 9	100	6	135	2048	35,636	478.8
case 10	60	9	15	43	66,924	870.7
case 11	80	9	15	269	54,424	754.8
case 12	100	9	15	549	45,387	604.7
case 13	60	9	75	1184	48,855	719.6
case 14	80	9	75	1738	34,801	511.1
case 15	100	9	75	1736	31,783	474.5
case 16	60	9	135	1063	54,937	789.3
case 17	80	9	135	1624	44,212	599.8
case 18	100	9	135	1517	36,577	497.2
case 19	60	12	15	−619	80,400	1014
case 20	80	12	15	−465	64,581	859.2
case 21	100	12	15	−206	47,021	643.6
case 22	60	12	75	521	50,080	741.1
case 23	80	12	75	1277	35,033	513.2
case 24	100	12	75	1300	32,178	482.1
case 25	60	12	135	287	55,177	818.5
case 26	80	12	135	1107	45,232	615.3
case 27	100	12	135	1014	37,242	508.9

Mass of current model is 7639.65 g; pick force of current model is 56,427 N; absorbed energy of current model is 840 J.

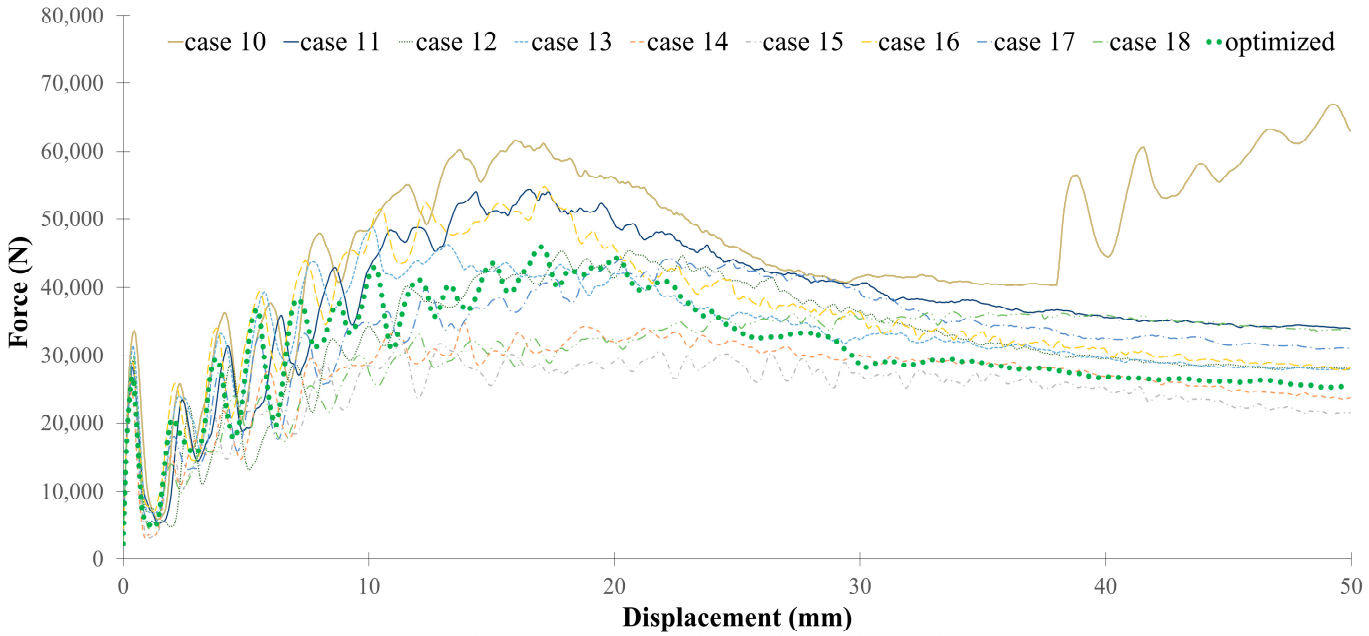

Figure 17. Force–displacement curves of cases 10–18 and the optimized model.

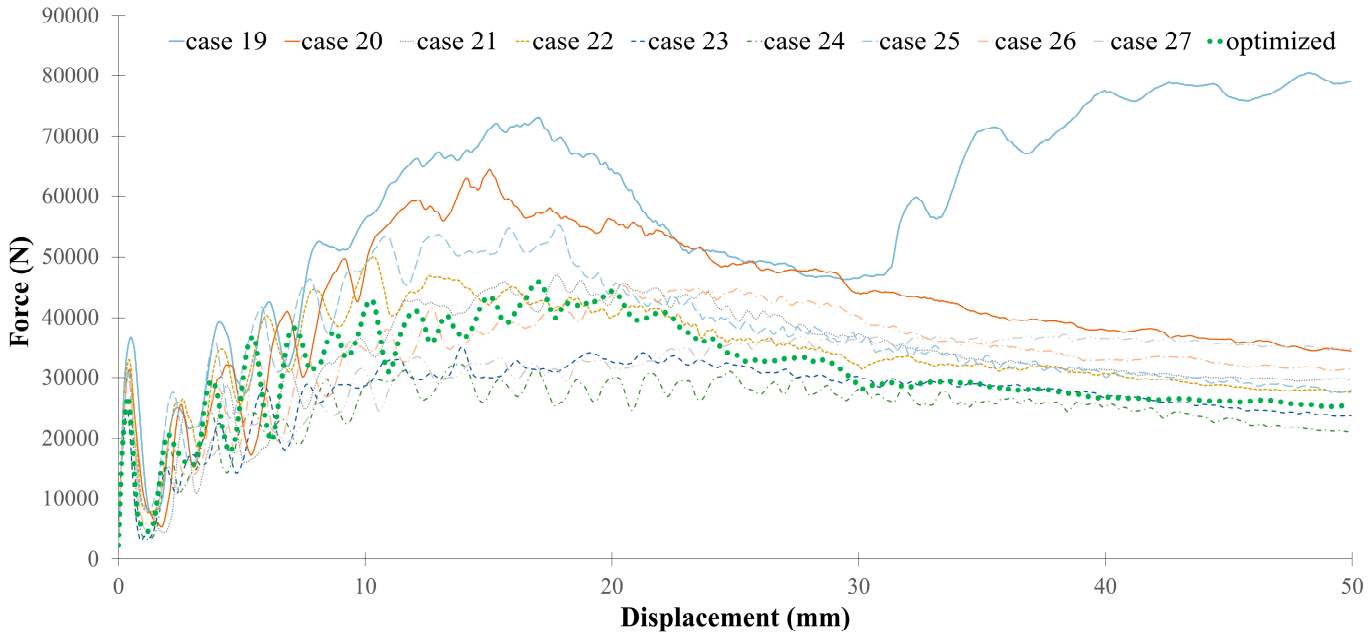

Figure 18. Force–displacement curves of cases 19–27 and the optimized model.

4.3. Results of the Sensitivity Matrix

A sensitivity matrix is used to determine values close to zero or parameters that have a negative effect, as shown in Figure 19.

	mass gain(g)	pick force(kN)	absorbed energy(kJ)
p1(edge length)	26.1%	-64.9%	-76.3%
p2(wall thickness)	-65.0%	24.5%	27.6%
p3(plane angle)	54.6%	-39.5%	-32.1%

Negative correlation

Positive correlation

Figure 19. Sensitivity matrix.

This optimization study aimed to simultaneously optimize three performance parameters that are critical in the design of the battery box side profile. These are the peak force (minimized), mass (minimized) and absorbed energy (maximized). The optimization process was performed over three design variables (p1, p2 and p3). The main objective of this study was to obtain optimal design solutions that balance these conflicting objectives.

4.4. Results of Optimization

First, the best-performing neural network models were identified, and their outputs were used as inputs in the next optimization phase. The regression plots shown in Figure 20

represent a statistical method used to model and predict the relationships between a dependent variable and one or more independent variables. The fitting curve uses regression analysis methods to find the mathematical model that best fits the data points. This analysis is a widely used tool for understanding the distribution and trend of a dataset, predicting future values or studying the relationships between variables.

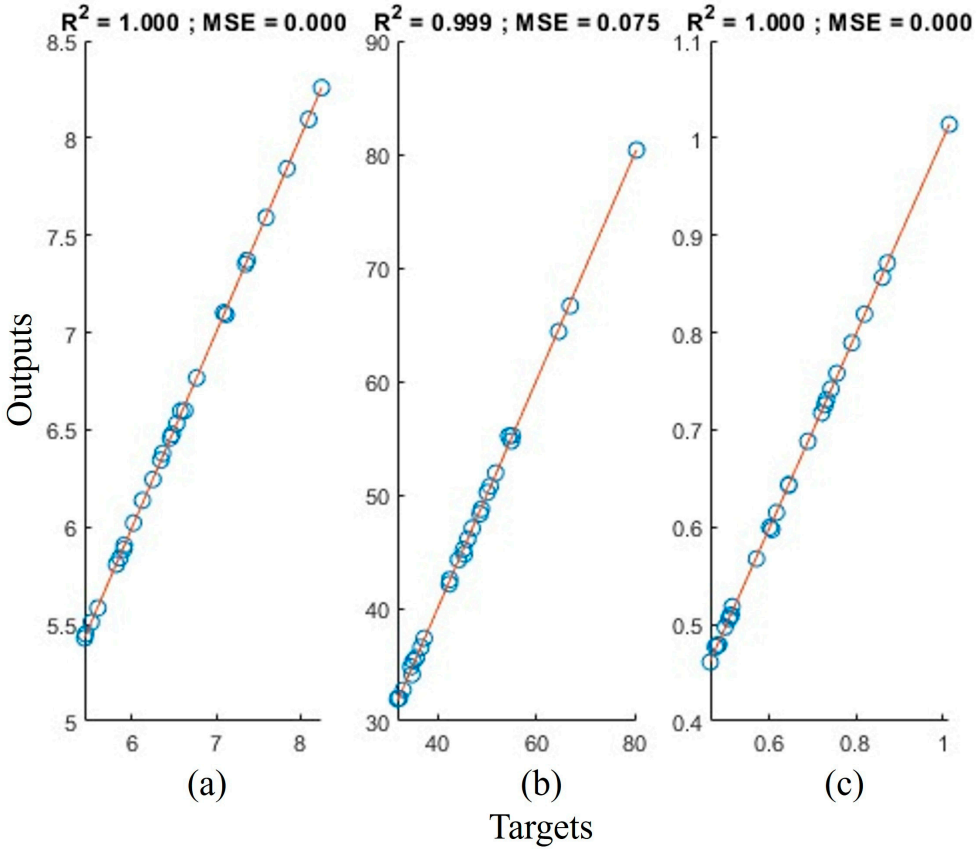

Figure 20. Regression plots of (**a**) mass (kg), (**b**) force (kN), and (**c**) absorbed energy (kJ).

Then, a multi-objective optimization method was applied using the best neural network models obtained. This optimization method aims to find the best combination of design variables in terms of crashworthiness and lightweight. This step was performed through MATLAB R2022b software, and the optimized design variables were defined.

The optimization process resulted in 35 Pareto-optimal solutions, as shown in Figure 21, which is an essential concept for identifying, analyzing and selecting optimal solutions in multi-objective optimization problems. After that, the TOPSIS method is implemented, and the function is equal to each objective, to reach the most balanced solution among these Pareto-optimal results.

As a result of the optimization, the optimal solution was observed at iteration No. 32, which is marked with a red point. The optimal parameters are given in Table 6.

Table 6. Optimum parameters.

Iteration No.	p1 (mm)	p2 (mm)	p3 (degree)	Peak Force (N)	Mass (g)	Absorbed Energy (J)
32	67.88	7.23	92.35	43,074.34	5812.27	633.65

The training process was carried out to minimize the mean square error (MSE). To improve the performance of the model and ensure the reliability of the results, 50 ANNs were trained with different initial weights. This approach reduced the risk of becoming

stuck in local minima and resulted in a more accurate model. As shown in Figure 22, R^2 and MSE values were continuously monitored to measure the test performance.

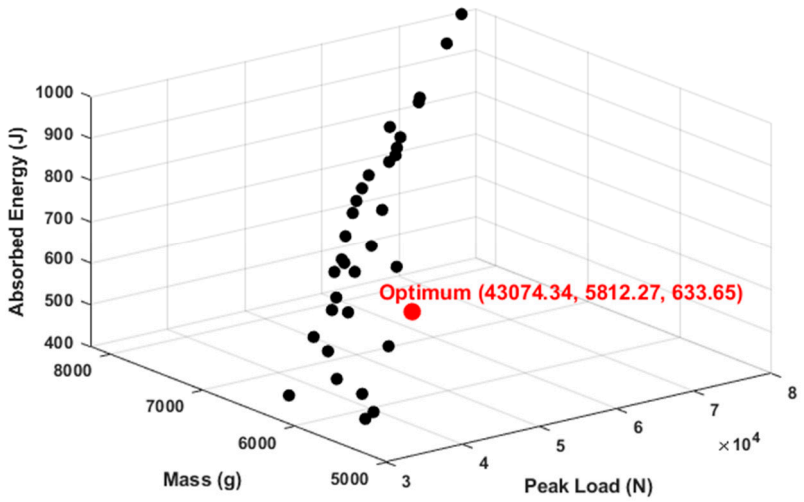

Figure 21. Three objective Pareto front curves with normalized data.

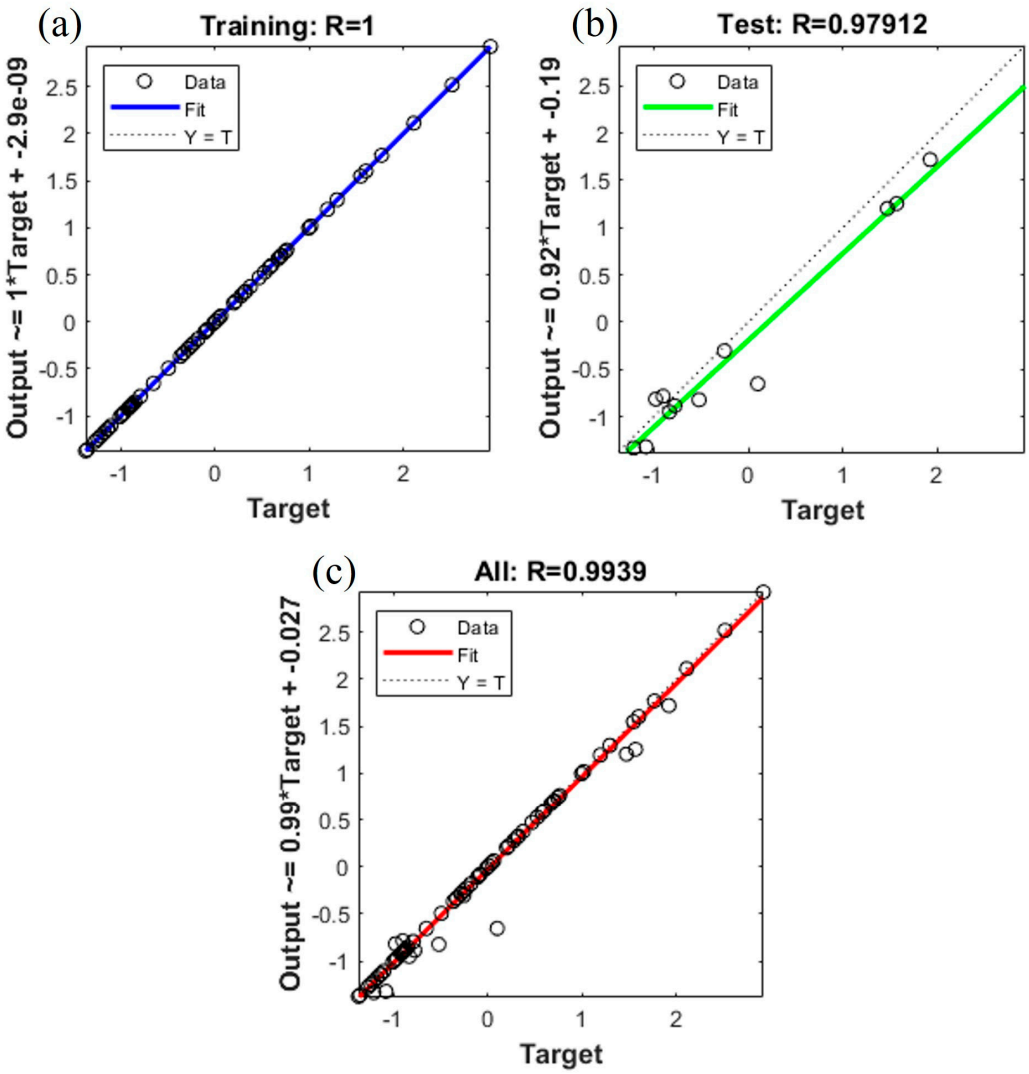

Figure 22. Multiple regression plots obtained from ANN: (**a**) training, (**b**) test, and (**c**) all.

The integrated approach applied in this study resulted in optimal solutions that balanced conflicting objectives. ANN models successfully model the complex relationships between design parameters and performance outputs. These models were evaluated via R^2 values and mean square error (MSE) metrics, and high levels of accuracy were achieved.

NSGA-II optimization effectively explores a large design space and produces several Pareto-optimal solutions. These solutions provide alternatives reflecting different design preferences. For example, some solutions minimize the peak load and mass while sacrificing absorbed energy, whereas others maximize absorbed energy while increasing other parameters.

The TOPSIS application made it possible to select the most balanced solution among the Pareto-optimal solutions. The optimal solution selected provided a reasonable balance between the three performance parameters.

The results obtained in this study are summarized in Table 7. The results of this study show that the proposed methodology is a powerful tool for solving complex engineering problems. This approach can be applied not only to optimize the battery side profile, but also to solve similar multi-objective optimization problems.

Table 7. Comparison of current design and optimized design.

	Current Design	**Optimized Design**
Material	Al 6082-T6	GFRP-GF800
Technology	EXTRUSION	PULTRUSION
Density (g/cm^3)	2.7	2
Weight (g)	7639.65	5812.27
Pick force (N)	56,427	49,909
Absorbed energy (J)	840	658
Specific energy absorption (SAE) (J/g)	0.10995	0.11321
Piece cost coefficient	1.628	1
Performance–cost ratio (SAE/piece cost)	0.06754	0.11321

According to the results of the analysis, the peak force was found to be 45,909 N, and the absorbed energy was found to be 658 J. When we compared the results with the MATLAB optimization results, 97% verification was obtained. The new design becomes 23.9% lighter and 38.6% cheaper. In total, a 1827 g weight reduction was achieved compared to the existing material and section geometry. Additionally, although the energy absorption up to 20 mm displacement was at a better level in the current model, the optimum design has better and 3% higher performance because the optimum design has less mass.

5. Conclusions

This study introduces an innovative approach that integrates ANN, NSGA-II, and TOPSIS methods to optimize the structural design of battery side profiles for electric vehicles. This approach effectively balances the conflicting objectives of minimizing weight, maximizing crash performance, and ensuring safety. This study demonstrated that a hybrid model combining honeycomb and auxetic structures achieved superior crashworthiness and lightweight performance.

In conclusion, this study's methodology offers a comprehensive solution not only for optimizing electric vehicle battery carriers but also for addressing similar multi-objective optimization challenges in engineering design. The use of ANN and NSGA-II in combination with decision-making tools such as TOPSIS proved effective in deriving balanced, high-performance design solutions that align with evolving needs in the automotive sector for safety, energy efficiency, and sustainability.

The proposed approach effectively addresses complex design challenges. The results of this study highlight several key findings:

- Innovative approach: the hybrid optimization methodology successfully combines ANN, NSGA-II, and TOPSIS, providing an effective strategy for balancing conflicting objectives such as weight reduction, crashworthiness, and overall safety.
- Optimization of conflicting objectives: The optimization effectively handles multiple conflicting objectives. The primary goals of this study focused on minimizing weight while maximizing crash performance, which is a key consideration in the automotive sector.
- Superior hybrid model: the optimized hybrid structure, which integrated honeycomb and auxetic elements, achieved significant improvements in crashworthiness and weight reduction, demonstrating the effectiveness of combining different configurations for enhanced performance.
- Weight reduction achievements: Compared with the current design, the optimization achieved a weight reduction of 1.8 kg per profile, corresponding to a 23.9% decrease in weight and a 38.6% cost reduction compared to the original design. These improvements highlight the approach's efficiency and cost-effectiveness, with 3% higher performance.
- Performance validation: the optimized design resulted in a peak force of 45,909 N and an absorbed energy of 658 J, with a verification accuracy of 97%, demonstrating the reliability and robustness of the proposed methodology.
- Material efficiency: this study emphasized the benefits of using GFRP-GF800 material over traditional aluminum, particularly in terms of weight reduction and energy efficiency, which are critical factors for electric vehicle applications.
- Versatility of the methodology: the methodology presented offers a versatile solution not only for optimizing electric vehicle battery carriers but also for addressing similar multi-objective optimization problems in engineering design.
- Implications for the automotive sector: this research aligns with the automotive industry's evolving needs for enhanced safety, energy efficiency, and sustainability, providing valuable insights for future structural optimizations in electric vehicles and other applications.

All these achievements obtained as a result of this study demonstrate that the approach developed is suitable for industrial applications and serves as a guide for future studies. In particular, with the widespread adoption of electric vehicles, the importance of such optimized lightweight structures will increase.

The findings also contribute significantly to the broader field of structural optimization, offering new perspectives on the integration of advanced materials and innovative geometries. The successful implementation of this methodology paves the way for future developments in automotive design, particularly in the context of electric vehicle safety and efficiency improvements.

Moreover, this study's comprehensive approach to optimization, combining multiple methodologies and considering various performance metrics, provides a robust framework that can be adapted to other engineering challenges beyond the automotive sector. This versatility and adaptability make the findings particularly valuable for researchers and practitioners working on similar complex engineering problems.

Critical reflection on this study's limitations is primarily associated with pultrusion. It is most suitable for producing parts with a constant cross-section, which restricts its capability to create complex or varying shapes, a significant drawback for certain applications. Achieving high-quality pultruded profiles necessitates meticulous control of various process variables, including fiber impregnation, resin viscosity, pulling speed, and curing

temperature. Any deviation can impact the final product's quality. While thermoplastic pultrusion offers benefits such as recyclability and toughness, it is less developed compared to thermoset pultrusion due to processing challenges and the need for further research and development. The pultrusion market is highly fragmented, with many small players. This fragmentation can impede innovation and the development of new applications due to limited resources.

In light of extensive research, it is evident that producing GFRP profiles with the specified properties under prototype conditions is not feasible. Therefore, a pultrusion mold must be created for the optimized section, and profiles must be manufactured according to the specified material mechanical properties and the matrix–fiber ratio outlined in the schematic representation section. Testing the battery carrier with all components is highly costly. The weakest part of the battery box measures 337 mm, which corresponds to the interval dimension of the inner beams. For the three-point flexural test, this distance is considered the interval between the lower supports. A 500 mm sample length is sufficient for testing. The upper crushing plate has a radius of 75 mm. The ISO 6469 standard can be applied for the test and the results can then be obtained and compared with simulation outcomes.

Author Contributions: M.A. contributed towards conceptualization, software, verification, visualization, data curation, formal analysis, investigation, methodology, writing—original draft, writing—review and editing, resources. M.İ.K. contributed towards conceptualization, methodology, writing—review and editing. All authors have read and agreed to the published version of the manuscript.

Funding: This research received no external funding.

Institutional Review Board Statement: Not applicable.

Informed Consent Statement: Not applicable.

Data Availability Statement: The data are presented within the article. For additional information or inquiries, please reach out to the corresponding author.

Conflicts of Interest: Author Muhammet Arslan was employed by the company Jaguar Land Rover. The remaining authors declare that the research was conducted in the absence of any commercial or financial relationships that could be construed as a potential conflict of interest.

References

1. Romero, C.A.; Correa, P.; Ariza Echeverri, E.A.; Vergara, D. Strategies for reducing automobile fuel consumption. *Appl. Sci.* **2024**, *14*, 910. [CrossRef]
2. Czerwinski, F. Current trends in automotive lightweighting strategies and materials. *Materials* **2021**, *14*, 6631. [CrossRef]
3. Grubisic, V. *Criteria and Methodology for Lightweight Design of Vehicle Components*; Fraunhofer LBF: Darmstadt, Germany, 1986.
4. Özel, S.; Karagöz, S.; Beytüt, H. Crashworthiness investigation of vehicle front bumper beam with different cross-sections under axial dynamic load. *Eur. J. Tech.* **2020**, *10*, 97–105. [CrossRef]
5. Dindar, Ç.; Beytüt, H.; Karagöz, S. Effect of heat treatment and cross section on the crashworthiness of 51CrV4 spring steel. *Uludağ Üniversitesi Mühendislik Fakültesi Derg.* **2019**, *24*, 477–488.
6. Alanazi, F. Electric vehicles: Benefits, challenges, and potential solutions for widespread adaptation. *Appl. Sci.* **2023**, *13*, 6016. [CrossRef]
7. Alternative Fuels Data Center. *Electric Vehicle Benefits and Considerations*; US Department of Energy: Washington, DC, USA, 2022.
8. Leal Filho, W.; Abubakar, I.R.; Kotter, R.; Grindsted, T.S.; Balogun, A.-L.; Salvia, A.L.; Aina, Y.A.; Wolf, F. Framing electric mobility for urban sustainability in a circular economy context: An overview of the literature. *Sustainability* **2021**, *13*, 7786. [CrossRef]
9. Cucinotta, F.; Raffaele, M.; Salmeri, F. A Well-to-Wheel Comparative Life Cycle Assessment Between Full Electric and Traditional Petrol Engines in the European Context. In *Advances on Mechanics, Design Engineering and Manufacturing III: Proceedings of the International Joint Conference on Mechanics, Design Engineering & Advanced Manufacturing, JCM 2020, 2–4 June 2020*; Springer International Publishing: Berlin/Heidelberg, Germany, 2021; pp. 188–193.
10. Verma, S.; Dwivedi, G.; Verma, P. Life cycle assessment of electric vehicles in comparison to combustion engine vehicles: A review. *Mater. Today Proc.* **2022**, *49*, 217–222. [CrossRef]

11. Belingardi, G.; Scattina, A. Battery pack and underbody: Integration in the structure design for battery electric vehicles—Challenges and solutions. *Vehicles* **2023**, *5*, 498–514. [CrossRef]
12. Zhang, J.; Ning, L.; Hao, Y.; Sang, T. Topology optimization for crashworthiness and structural design of a battery electric vehicle. *Int. J. Crashworthiness* **2021**, *26*, 651–660. [CrossRef]
13. Hao, F.; Lu, X.; Qiao, Y.; Chen, X. Crashworthiness analysis of electric vehicle with energy-absorbing battery modules. *J. Eng. Mater. Technol.* **2017**, *139*, 021022. [CrossRef]
14. McCafferty, G. Electric vehicle battery crashworthiness considerations. In Proceedings of the 30th IEEE Vehicular Technology Conference, Dearborn, MI, USA, 15–17 September 1980; pp. 255–260.
15. Mudassir, M.; Tarlochan, F.; Mansour, M.A. Nature-Inspired cellular structure design for electric vehicle battery compartment: Application to crashworthiness. *Appl. Sci.* **2020**, *10*, 4532. [CrossRef]
16. Mushtaq, M.; Satish, S. A Review on Crashworthiness and Cooling Models for Lithium-Ion Batteries in Electric Vehicles. In *Advances in Lightweight Materials and Structures: Select Proceedings of ICALMS 2020*; Springer: Berlin/Heidelberg, Germany, 2020; pp. 75–84.
17. Wang, W.; Dai, S.; Zhao, W.; Wang, C.; Ma, T. Design optimization of a novel negative Poisson's ratio non-module battery pack system considering crashworthiness and heat dissipation. *Compos. Struct.* **2021**, *275*, 114458. [CrossRef]
18. Xiong, Y.; Pan, Y.; Wu, L.; Liu, B. Effective weight-reduction-and crashworthiness-analysis of a vehicle's battery-pack system via orthogonal experimental design and response surface methodology. *Eng. Fail. Anal.* **2021**, *128*, 105635. [CrossRef]
19. Zhao, G.F.; Liu, M.M.; Li, Y. Safety research and lightweight design of electric vehicle battery protection device. *Adv. Mater. Res.* **2013**, *724*, 1366–1373. [CrossRef]
20. Obradovic, J.; Boria, S.; Belingardi, G. Lightweight design and crash analysis of composite frontal impact energy absorbing structures. *Compos. Struct.* **2012**, *94*, 423–430. [CrossRef]
21. Witteman, W.J. Improved vehicle crashworthiness design by control of the energy absorption for different collision situations. Ph.D. Thesis, Eindhoven University of Technology, Eindhoven, The Netherlands, 1999.
22. Özel, S.; Beytüt, H.; Karagöz, S. Effect of forming history on crashworthiness of a spot-welded and double-hat elliptical thin-walled tube. *Eur. J. Tech.* **2019**, *9*, 275–285. [CrossRef]
23. Gao, D.; Yao, B.; Chang, G.; Li, Q. Multi-Objective Optimization Design of Vehicle Side Crashworthiness Based on Machine Learning Point-Adding Method. *Appl. Sci.* **2022**, *12*, 10320. [CrossRef]
24. Wang, D.; Xie, C.; Liu, Y.; Xu, W.; Chen, Q. Multi-objective collaborative optimization for the lightweight design of an electric bus body frame. *Automot. Innov.* **2020**, *3*, 250–259. [CrossRef]
25. Li, Z.; Duan, L.; Cheng, A.; Yao, Z.; Chen, T.; Yao, W. Lightweight and crashworthiness design of an electric vehicle using a six-sigma robust design optimization method. *Eng. Optim.* **2019**, *51*, 1393–1411. [CrossRef]
26. Maiti, S.; Islam, M.R.; Uddin, M.A.; Afroj, S.; Eichhorn, S.J.; Karim, N. Sustainable fiber-reinforced composites: A Review. *Adv. Sustain. Syst.* **2022**, *6*, 2200258. [CrossRef]
27. Rajak, D.K.; Wagh, P.H.; Linul, E. Manufacturing technologies of carbon/glass fiber-reinforced polymer composites and their properties: A review. *Polymers* **2021**, *13*, 3721. [CrossRef] [PubMed]
28. Baran, I.; Akkerman, R.; Hattel, J.H. Material characterization of a polyester resin system for the pultrusion process. *Compos. Part B Eng.* **2014**, *64*, 194–201. [CrossRef]
29. Bechtold, G.; Wiedmer, S.; Friedrich, K. Pultrusion of thermoplastic composites-New developments and modelling studies. *J. Thermoplast. Compos. Mater.* **2002**, *15*, 443–465. [CrossRef]
30. Britnell, D.J.; Tucker, N.; Smith, G.; Wong, S. Bent pultrusion—A method for the manufacture of pultrudate with controlled variation in curvature. *J. Mater. Process. Technol.* **2003**, *138*, 311–315. [CrossRef]
31. Kennedy, K.C.; Kusy, R.P. UV-cured pultrusion processing of glass-reinforced polymer composites. *J. Vinyl Addit. Technol.* **1995**, *1*, 182–186. [CrossRef]
32. Novo, P.; Silva, J.F.; Nunes, J.; Marques, A. Pultrusion of fibre reinforced thermoplastic pre-impregnated materials. *Compos. Part B Eng.* **2016**, *89*, 328–339. [CrossRef]
33. Volk, M.; Yuksel, O.; Baran, I.; Hattel, J.H.; Spangenberg, J.; Sandberg, M. Cost-efficient, automated, and sustainable composite profile manufacture: A review of the state of the art, innovations, and future of pultrusion technologies. *Compos. Part B Eng.* **2022**, *246*, 110135. [CrossRef]
34. Talabi, S.I.; Tobin, J.; Strom, B.; Brownstein, I.; Kunc, V.; Hassen, A.A. Recent and future developments in pultrusion technology with consideration for curved geometries: A review. *Compos. Part B Eng.* **2024**, *283*, 111678. [CrossRef]
35. Simpson, J.; Kazancı, Z. Crushing investigation of crash boxes filled with honeycomb and re-entrant (auxetic) lattices. *Thin-Walled Struct.* **2020**, *150*, 106676. [CrossRef]
36. Buljak, V.; Cocchetti, G.; Cornaggia, A.; Maier, G. Parameter identification in elastoplastic material models by Small Punch Tests and inverse analysis with model reduction. *Meccanica* **2018**, *53*, 3815–3829. [CrossRef]

37. Nasrullah, A.I.H.; Santosa, S.P.; Dirgantara, T. Design and optimization of crashworthy components based on lattice structure configuration. *Structures* **2020**, *26*, 969–981. [CrossRef]
38. Li, D.; Qin, R.; Xu, J.; Zhou, J.; Chen, B. Topology optimization of thin-walled tubes filled with lattice structures. *Int. J. Mech. Sci.* **2022**, *227*, 107457. [CrossRef]
39. Xin, H.; Liu, Y.; Mosallam, A.S.; He, J.; Du, A. Evaluation on material behaviors of pultruded glass fiber reinforced polymer (GFRP) laminates. *Compos. Struct.* **2017**, *182*, 283–300. [CrossRef]
40. Pranathi, K.; Ayub, S.M.A.; Paul, C. Composite Laminates with Epoxy Resin and E-Glass Fibers: Analysis of Mechanical Properties. *J. Phys. Conf. Ser.* **2024**, *2837*, 012008. [CrossRef]
41. Rana, R.; Rana, S.; Purohit, R. Characterization of properties of epoxy sisal/glass fiber reinforced hybrid composite. *Mater. Today Proc.* **2017**, *4*, 5445–5451. [CrossRef]
42. John, K.; Naidu, S.V. Tensile properties of unsaturated polyester-based sisal fiber–glass fiber hybrid composites. *J. Reinf. Plast. Compos.* **2004**, *23*, 1815–1819. [CrossRef]
43. Sakib, M.N.; Iqba, A.A. Epoxy based nanocomposite material for automotive application-a short review. *Int. J. Automot. Mech. Eng.* **2021**, *18*, 9127–9140. [CrossRef]
44. Bilmez, S.; Taşdemirci, A. Experimental and Numerical Investigation of Energy Absorption Characteristics of a E-Glass/Epoxy Crash Box. *J. Phys. Conf. Ser.* **2024**, *2725*, 012004. [CrossRef]
45. Garg, R.; Babaei, I.; Paolino, D.S.; Vigna, L.; Cascone, L.; Calzolari, A.; Galizia, G.; Belingardi, G. Predicting composite component behavior using element level crashworthiness tests, finite element analysis and automated parametric identification. *Materials* **2020**, *13*, 4501. [CrossRef]
46. Hu, Q.; Lu, G.; Tse, K.M. Compressive and tensile behaviours of 3D hybrid auxetic-honeycomb lattice structures. *Int. J. Mech. Sci.* **2024**, *263*, 108767. [CrossRef]
47. Jafari, A.; Ashrafi, H.; Bazli, M.; Ozbakkaloglu, T. Effect of thermal cycles on mechanical response of pultruded glass fiber reinforced polymer profiles of different geometries. *Compos. Struct.* **2019**, *223*, 110959. [CrossRef]
48. Ingrole, A.; Hao, A.; Liang, R. Design and modeling of auxetic and hybrid honeycomb structures for in-plane property enhancement. *Mater. Des.* **2017**, *117*, 72–83. [CrossRef]
49. Carakapurwa, F.E.; Santosa, S.P. Design optimization of auxetic structure for crashworthy pouch battery protection using machine learning method. *Energies* **2022**, *15*, 8404. [CrossRef]
50. Beytüt, H.; Özbeyaz, K.; Temiz, Ş. A Novel Hybrid Die Design for Enhanced Grain Refinement: Vortex Extrusion–Equal-Channel Angular Pressing (Vo-CAP). *Appl. Sci.* **2025**, *15*, 359. [CrossRef]
51. Biharta, M.A.S.; Santosa, S.P.; Widagdo, D. Design and optimization of lithium-ion battery protector with auxetic honeycomb for in-plane impact using machine learning method. *Front. Energy Res.* **2023**, *11*, 1114263. [CrossRef]
52. Moré, J.J. The Levenberg-Marquardt algorithm: Implementation and theory. In *Numerical Analysis: Proceedings of the Biennial Conference Held at Dundee, 28 June–1 July 1977*; Springer: Berlin/Heidelberg, Germany, 1978; pp. 105–116.
53. Deb, K.; Pratap, A.; Agarwal, S.; Meyarivan, T. A fast and elitist multiobjective genetic algorithm: NSGA-II. *IEEE Trans. Evol. Comput.* **2002**, *6*, 182–197. [CrossRef]
54. Wang, C.; Yoon, K. Multiple attribute decision making. *Lect. Notes Econ. Math. Syst.* **1981**, *404*, 287–288.
55. Zhao, Y.; Zhai, X. Bending strength and design methods of the 6082-T6 aluminum alloy beams with circular hollow sections. *Structures* **2020**, *26*, 870–887. [CrossRef]
56. Zhao, Y.; Zhai, X.; Sun, L. Test and design method for the buckling behaviors of 6082-T6 aluminum alloy columns with box-type and L-type sections under eccentric compression. *Thin-Walled Struct.* **2016**, *100*, 62–80. [CrossRef]

Disclaimer/Publisher's Note: The statements, opinions and data contained in all publications are solely those of the individual author(s) and contributor(s) and not of MDPI and/or the editor(s). MDPI and/or the editor(s) disclaim responsibility for any injury to people or property resulting from any ideas, methods, instructions or products referred to in the content.